29 April 2023

Semi-monolithic meta-scintillator simulation proof-of-concept, combining accurate DOI and TOF

Georgios Konstantinou[1], Lei Zhang, Antonio Gonzalez, Paul LECOQ

1. Multiwave Metacrystal

Abstract

Presentation of simulation results on a new metascintillator concept (semi-monolithic) combining state-of-the art timing resolution and depth-of-interaction, with the application of neural networks to provide accurate estimations of energy sharing and energy of interaction.

Keywords

, depth of interaction, , time of flight, metascintillators, nuclear engineering, positron emission tomography, scintillators, semi-monolithic

Semi-monolithic meta-scintillator simulation proof-of-concept, combining accurate DOI and TOF

Georgios Konstantinou, *Member, IEEE,* Lei Zhang, Daniel Bonifacio, Riccardo Latella, Jose Maria Benlloch, Antonio J. Gonzalez, *Member, IEEE* and Paul Lecoq, Senior *Member, IEEE*

***Abstract*— Metascintllators arrangements have shown to achieve an equivalent CTR of 200 ps for BGO-plastic and 140 ps for LYSO-plastic sets. In this paper, we examine a novel architecture: The idea is to slice a slow scintillator (BGO or LYSO) into thin slabs read out by an array of SiPM in the semimonolithic manner providing depth-of-interaction (DOI) information; and interleave them with thin segmented fast scintillators (plastic EJ232 or EJ232Q) read out by single SiPMs as in pixelated designs, providing pixelated level coincidence time resolution (CTR), in what we call a semi-monolithic meta-scintillator (SMMS). We thus combine layers of slow scintillator of dimension 0.3x25.5x(15 or 24) mm^3 and layers of fast scintillator of dimensions 0.1x3.1x(15 or 24) mm^3 in a Monte Carlo Gate platform to investigate the performance of this new type of semi-monolithic detector. It is shown that the time resolution of SMMS is equivalent to that of single metapixels of the same configuration. In particular, 15 mm deep LYSO based SMMS led to CTR 121 ps, before implementation of timewalk correction (107 ps CTR). Same dimensions for BGO based SMMS led to CTR of 241 ps, a 15% deviation from metapixel experimental results. Further to this timing study, we expand the study to application of neural networks on the photon distributions and timestamps recorded at the SiPM array. This leads to determination of the DOI with < 3mm precision and 0.85 confidence level in the best scenario and more than 2 standard deviations precision in reconstructing energy sharing and energy of interactions. Overall, neural network prediction capabilities, taking advantage of enhanced understanding of the photon distribution, exceed those of the standard energy calculation through addition of numbers of detected photons or any analytic approach on energy sharing.**

***Index Terms*— Positron emission tomography, time of flight, depth of interaction, scintillators, semi-monolithic, metascintillators**

I. Introduction

POSITRON Emission Tomography (PET) has reached a level of maturity as an imaging technique with the lancing of new scanners such as the United Imaging total body PET [1] and Siemens Quadra [2]. Current instrumentation developments mostly concentrate to enhance the overall sensitivity an signal-to-noise ratio (SNR) of the detector. Improved SNR directly translates to reduce examination time and radiation dose, improved image quality, or a combination of both. Apart from the improvement on subject coverage achieved with the aforementioned designs, there are three main directions to achieve this target.

The first corresponds to using scintillating materials with high gamma stopping power, improving sensitivity through improving the number of recorded coincidences for a given amount of time and activity [3]. The second is related to improving the spatial resolution of the detector; this leads to higher granularity on detection and image through reduction of the transverse dimensions of the lines-of-response (LOR) [4]. To be noted, spatial resolution of the detector corresponds to the tri-dimensional precision of gamma interaction localization, including both x-y coordinates and gamma depth-of-interaction (DOI), with the latter significantly affecting image quality away from the center of the field-of-view (FOV). The third direction reflects the improvement on image SNR by implementing time-of-flight (TOF) information on coincidences. There is a reverse square root relation between effective sensitivity and detector coincidence timing resolution (CTR) due to the segmentation of the LOR along its direction [5].

Further to these directions, combinatory improvements of detector specifications can provide synergistic added value to its effective sensitivity. As an example, we look in detail into the combination of DOI and TOF, which enhances detector effective sensitivity, through several mechanisms. On top of the TOF improvement, DOI adds the aforementioned reduction of LOR cross-section, increases the number of LORs due to the addition of more resolvable detector elements, and finally reduces or eliminates the parallax error [6]. On top of all these improvements, taking-into-account that DOI is the predominant mechanism deteriorating CTR for longer crystals, DOI knowledge allows mitigating this effect through a DOI-driven time-walk correction [7].

Parallax error can be particularly significant for architectures where FOV size is similar to the diameter of the object-of-interest, with main examples the designs of brain and preclinical PETs [4]. The same applies in other single organ architectures. Scanners with object-of-interest of up to 25 cm cannot easily apply TOF, as they would require detectors with coincidence time resolution (CTR) better than 400 ps for even a marginal TOF improvement; nevertheless, the development of cost-effective detectors capable of CTR around 200 ps and the expectation of system-level scalable designs in the near future [8] with timing close or better than 100 ps, brings the

Submitted for review on the 10th of March 2023. The two first authors contributed equally. This work is based on the concept initiated in the framework of the ERC Advanced Grant TICAL (338953) funded by the European Research Council. This work was supported in part by the European Research Council (ERC) under the European Union's Horizon 2020 research and innovation program (grant agreement No 695536): 4D-PET. This work did not involve human subjects or animals in its research.

G. Konstantinou (georgios@metacrystal.ch), R. Latella, and P. Lecoq are with both Multiwave Metacrystal, 34 Route de la Galaise, 1228, Geneva, Switzerland and Instituto de Instrumentación para Imagen Molecular (I3M), Centro Mixto CSIC—Universitat Politècnica de València, 46022 Valencia, Spain

L. Zhang (Lei@metacrystal.ch) is with Multiwave Metacrystal S.A.

D. Bonifacio is with Instituto de Pesquisas Energéticas e Nucleares - IPEN Avenida Prof. Lineu Prestes, 2242 - Cidade Universitária - bairro Butantã , Sao Paolo, Brazil.

A.J. Gonzalez and J.M. Benlloch are with I3M.

combination of DOI with TOF in the forefront of development of new PET designs. As an example, we showcase in figure 1 a human brain PET with 1.5 mm radial spatial resolution, only two DOI levels and 5 cm (330 ps) TOF resolution. For each coincidence, the SNR is improved by approximately 2 due to LOR lateral dimensions and another 2.5 times due to TOF.

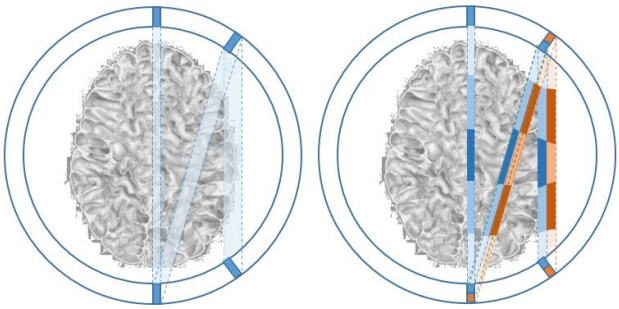

Fig. 1. Example of the added value when using DOI and TOF: three simple LORs (left-light blue) are truncated transversely (light-blue and orange) due to DOI information and longitudinally with the use of TOF (variations of blue and orange), significantly improving the amount of information on the location of each annihilation, for each coincidence pair.

One potential way to overcome the impasse between good timing and sufficient gamma absorption efficiency is the concept of metascintillators [5]. In the first generation, we combined a high-Z but slower compound, such as BGO or LYSO, with fast but light ones, such as BaF_2 and plastic. Herein, experimental results show agreement when compared to simulation. However, until now only pixel configurations having 1-to-1 matching between metascintillator and silicon photomultiplier (SiPM) have been tested. While timing is optimal under such conditions, there is no DOI information.

In this work, we present the simulated proof-of-concept of the added capabilities that the structuration of metascintillators can offer; through a design that slightly simplifies the metascintillating stack. Therefore, it is possible to reduce the amount of components to be included, with the further advantage of adding DOI capabilities. We use a novel, neural network (NN)-based approach to analyze event signatures and retrieve the maximum of information from several channels, while proposing ways to improve detector specifications with data driven corrections.

II. Materials and Methods

A. Semi-monolithic metascintillator (SMMS) principle

A novel approach in achieving good DOI performance with good general detector characteristics is the semi-monolithic approach [9]. Herein, scintillators are cut in such dimensions as to be readable by a 1-dimensional array of photosensors. Semi-monolithic, in this sense, corresponds to 1 lateral dimension being monolithic and 1 lateral dimension being pixelated.

The result of this is that the most of the photosensors of the 1D array are illuminated for each event. The relative number of photons detected in each SiPM can be considered as a scintillation light distribution. The statistical characteristics of this distribution allows precise localization along the monolithic and DOI positions of the impinging event. The advantage of semi-monolithic designs is a better event positioning than the pixelated, while having generally better timing than the monolithic.

This mechanism has been expanded to metascintillators. A potential design is to keep the semi-monolithic structure for the slow, high-Z component of the metascintillator. However, the fast material can remain segmented in the same dimensions as in pixelated designs. This means that the light from the slow material can be used to decode the y-z position of the impact position. However, the pixelated nature of the fast material allows fast photons to be contained in it and provide timing with the same availability as in the pixelated approaches. In this case, the semi-monolithic meta-scintillator (SMMS) is expected to combine monolithic capabilities of DOI, pixelated metascintillator quality TOF and sufficient stopping power (fig. 2).

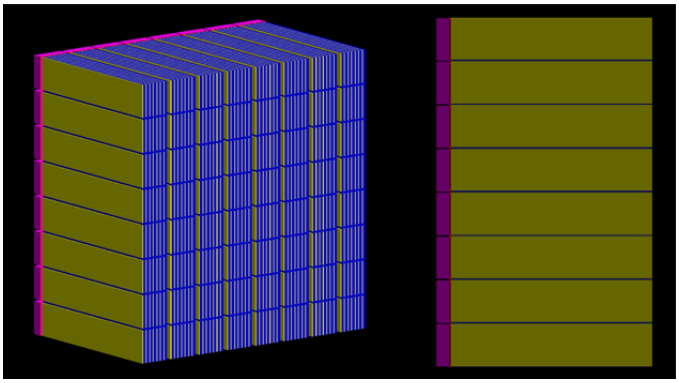

Fig. 2: Concept and simulation model of an 8x8 SiPM equivalent SMMS in orthographic (left) and side (right) view: (yellow) fast scintillator stripes 0.1x3.1x15.0 mm^3, (blue) 0.3x25.5x15.0 mm^3 slow scintillator semi-monolithic slabs, (magenda) optical grease and (violet) SiPM.

B. Computational and simulation concept

To test the aforementioned hypothesis, the Monte-Carlo platform GATE, based on GEANT4 was used [10]. An end-to-end pipeline was built, including 3 sequential steps: data generation/collection; data processing and preparation; model training and optimization. A python-based wrapper has been implemented to link the simulator, with a fully parameterizable set of variables customizing the geometry and materials of the simulated SMMS. This modular approach allows tests of different scenarios on the same raw or the same pre-processed data, without the requirement of rerunning the whole pipeline.

To reduce the computational complexity of the simulation, a single SMMS array coupled to 8 SiPMs was implemented. The resulting timing distributions correspond to detector time resolution (DTR) rather than coincidence time resolution (CTR); gammas are emitted at local time t_0=0. To compare the timing capabilities of SMMS based on pixelated approaches, the same simulation was made on a single metascintillator pixel. The calculation of the corresponding detector CTR, when two detectors of same DTR are placed in coincidence, is following the equation $CTR = DTR \times \sqrt{2}$ [5].

C. Simulator characteristics

The array is illuminated from a distance of 50 mm, with a cone beam of 511 keV gammas that is wide enough to cover a 3x3 mm^2 section of the SMMS, roughly corresponding to the

scintillating material over each SiPM. The beam is moved in 3 mm steps (Fig. 3).

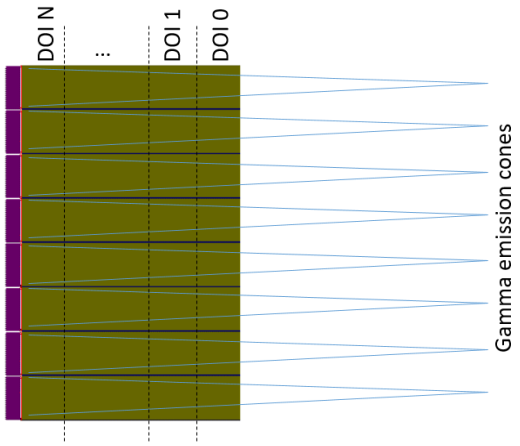

Fig. 3; Simplified sketch of the simulated architecture, side view. DOI levels are counted from the gamma emission direction inwards. The gamma emission cones (blue lines) are not in scale.

The simulation includes both nuclear and optical packages. Cherenkov photon production has not been included. For the nuclear part, in order to perform a precise simulation of the energy sharing in the metascintillator, particle energy cuts were reduced to maximum convergence point, corresponding to 0.001 mm. For the optical part of the simulation, precise scintillation photon wavelength spectra were input, based on vendor-provided information [11-14]. The wavelength distribution is of particular interest in the case of metascintillators, as they combine more than one material leading to a complex wavelength distribution, which interplays with the photon detection efficiency (PDE) distribution of the SiPM. Furthermore, optical grease and an absorption model of the photosensor was added. The SiPM considered the aforementioned wavelength-sensitive PDE (see Fig. 4), according to the specifications and size of FBK NUV, with 40 um SPAD size.

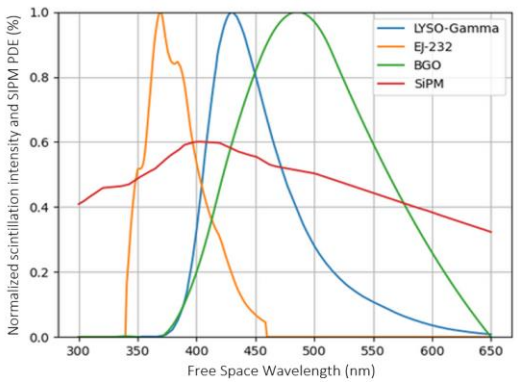

Fig. 4; Wavelength distribution of the model used for scintillator emission and SiPM PDE, as retrieved from corresponding sources (Saint-Gobain, Eljen and FBK).

No special wrapping has been considered for the whole volume of the SMMS, meaning that the reflection/transmission behavior of optical photons will be following the Snell's law of idealized (polished) surface. The reflectance depends completely on the refractive index of corresponding materials. In these simulations, the refractive index of LYSO and BGO are set to 1.81 and 2.15, respectively. Finally, the coupling with photon detector is modeled by optical grease with refractive index of 1.5 and 0.1 mm thickness. The SiPM volume has been included but no material was assigned.

D. Simulated Geometries

The scintillator design that was simulated was based on a realistic combination of high-Z and fast materials, which leads to gamma sensitivity similar to the designs found in existing commercial systems. Layers of slow scintillator (BGO, LYSO) with sections coupled to the SiPM of 0.3x25.5 mm^2 and layers of fast scintillator (EJ232, EJ232Q) with areas of 0.1x3.1 mm^2 are used. These match the side dimension of 8 and 1 SiPM, respectively, including 0.1 mm space between them (Fig. 2). They are combined in structures of either 15 mm height, applicable for preclinical studies, or 24 mm height, relevant for clinical PET designs. Each SMMS of ~3x25.5 mm^2 area is externally wrapped with Teflon, modeled as such in GATE. The simulated geometries are listed in table I. For clarity, different scenarios will be referred to through their index number from now on.

TABLE I

SMMS SIMULATED SCENARIOS

GEOMETRY SCENARIO	MATERIALS	LENGTH
I	BGO-EJ232	15 mm
II	LYSO:Ce-EJ232Q	15 mm
III	BGO-EJ232	24 mm
IV	LYSO:Ce-EJ232Q	24 mm

An added element of these combinations is that they allow examination of extreme scenarios of energy sharing and measured energy correlation. The BGO-EJ232 produce almost the same light yield, meaning that separating the events that are fully absorbed in the system is possible through isolation of the photopeak. In contrast, LYSO:Ce and EJ232Q have almost an order of magnitude difference in their light yields, meaning that the final measured energy, corresponding to the effective number of photons produced, is strongly dependent on the energy sharing. This makes isolation of fully absorbed events significantly more complicated.

While the full waveforms of photon detection per SiPM are available, this analysis is focused on information which can be realistically retrieved in a scaled up system. The purpose for this is to demonstrate that not only more complex solutions (full waveform or waveform feature analysis), presented previously [15] carry energy sharing information. In this work we consider the total number of photons (TNP) and first photon arrival time (FPAT). These are surrogates of SiPM charge and a low threshold timestamp, respectively.

To further expand the precision of the simulation, the single photon time resolution (SPTR) of the SiPM is added. This is given as a standard deviation value corresponding to the values found in literature [14]. While this is parametrizable, in the current modelling, a value of 70 ps FWHM (30 ps standard deviation) was used.

E. Post-processing

GATE produces a vast list of information corresponding to every particle interaction, including the several thousand

optical photons for each gamma event. In order to create an easy to use list of interactions, the majority of particles from the list is decimated, keeping only the information that is relevant to the particular experiment.

First, the spatial and temporal coordinates of the initial gamma interaction are recorded. Also, interactions concerning the extent of energy being absorbed by the scintillator are recorded in three categories: scattered, photoelectric and fully contained scattered. The last category corresponds to Compton scattering being the initial interaction, but with the process finishing with a photoelectric absorption at a different location of the scintillator. This is important as a secondary energy sharing mechanism, potentially producing errors concerning the initial location of interaction and accurate characterization of the LOR. Finally, the respective amount of energy deposition in the two materials is also stored for each event.

It has been demonstrated that significant information, such as the DOI, can be retrieved through the relative charges among the SiPM of a semi-monolithic array [9]. The respective timestamps are perhaps less useful in determining the DOI, but can be vital in calculating the extent of energy sharing. The mechanism of this corresponds to the 1-to-1 matching of fast material stripes to SiPMs, which leads to the produced prompt photons being recorded significantly earlier than those of the slow material which are distributed over the whole array.

F. NN application

The main purpose of the structuration of SMMS is on retrieving DOI information from the distribution of optical photon detection. Based on the processed simulation results, we have firstly trained different machine learning models to predict the DOI.

Initially, we focused on scenarios I and II, using only number of photons information. The input of the model is a one-dimensional array containing 8 numerical entries. The output can be an integer value indicating the DOI category in case of a classification problem, or a real number representing the coordinate of gamma interaction along the crystal longitudinal direction in case of a regression problem. To choose a suitable machine learning model, the Pycaret Python library for model benchmarking and hyperparameters training was used [16]. We firstly compared the accuracy of different common classifiers such as multiple layer perceptron (fully-connected NN) [17], random forest classifier [18] and extreme gradient boosting [19]. When tested on data from scenarios I and II, the fully-connected NN was the optimal strategy in all cases. Then, hyperparameters of previously obtained NN models were automatically tuned with Pycaret to achieve optimal prediction accuracy. Finally, the resulting NN model was reimplemented with the Tensorflow Python library for test and analysis [20].

In the case of classification, the average quality of prediction is calculated as the ratio of correctly predicted events over all events. The visual tool to facilitate understanding of the process is a confusion map of real versus predicted values. The regression problem can be considered as a classification with infinitesimal category size. Thus, the corresponding confusion map is a 2D scatter plot of the true vs predicted values.

Calculating the quality of prediction in these terms deviates slightly from the traditional approach of plotting, fitting a gaussian and providing a full-width at half maximum (FWHM) value as the figure of merit. For the results of NN prediction to be comparable with traditional scenarios, we set a threshold of 0.75 successful prediction. This corresponds directly to the FWHM of a Gaussian, where roughly 75% of its values are found within this width. At the same time, the precision of accuracy is found through the performance of the models in key parameter indicators (KPI). In the case of DOI, such KPI can be the extent of improvement of DTR with the application of relevant time-walk corrections [7], or that of energy resolution [21], given that the causal relation between DOI accuracy and DTR or energy resolution is well established.

During the second phase, we first repeat the same model training and testing process on the datasets from scenarios III and IV. Same as before, these models are expected to predict DOI. In addition to the 8 TNP, we also feed the 8 FPAT, one per SiPM for each gamma event. These additional features can improve the DOI prediction as there is a strong correlation between Gamma interaction position and optical photon traveling time. This task was focused on in scenarios III and IV, due to the limited performance achieved with the approach followed for scenarios I and II. Furthermore, all simulation data are being used without consideration on the amount of data corresponding to each class. This was due to the significant number of classes and the limitation in data production. Nevertheless, it is expected from the exponential form of beer-lambert law [15], that the majority of events take place closer to the gamma receiving side (DOI layer 0), leading to an imbalanced dataset. A different approach corresponds to balancing training data, meaning that each class is represented by the same number of events. This is done by building a training dataset limited in size by the amount corresponding to the least populated class.

After the work on DOI estimation, 2 fully-connected NN models have also been trained to predict the total energy deposited inside fast scintillation material (EJ232 or EJ232Q) and slow scintillation material (BGO or LYSO). This was recorded including energy by primary gamma and secondary particles, for each event. Using this true, known value of energy sharing was useful to predict through the application of NN both energy sharing extent, as well as the energy of interaction. This second step of phase one applied only on crystals of scenarios III and IV and considers simulation results of not only 511keV events but also scattering, for both training and testing dataset. The approximation of energy deposition values can serve for 2 uses. Firstly, the sum of both outputs gives total energy deposition, allowing to discriminate fully absorbed from scattered events, allowing safe allocation of a LOR at system level. Secondly, the proposition of energy deposition in fast and slow scintillation material provides the energy sharing ratio of metascintillator [5].

III. RESULTS

A. Distribution of photoelectric events

In figure 5 the distribution of photoelectric events is shown for scenarios I (top) and II (bottom), and for different DOIs. This is presented as a function of the total number of detected photons (x axis) and 3 mm DOI (color code, 0 at gamma entry side). Scenario I leads to a distribution ranging significantly, between 750 and 1500 photons, for the same impinging energy

(511 keV). Scenario II has a range as expected from previously simulated energy sharing distribution [5], with some events with significant energy in the fast material reaching down to one sixth of the maximum value of the histogram. Due to the higher light yield in LYSO:Ce, features of this histogram are better defined, as understood by the narrow width of the main peak.

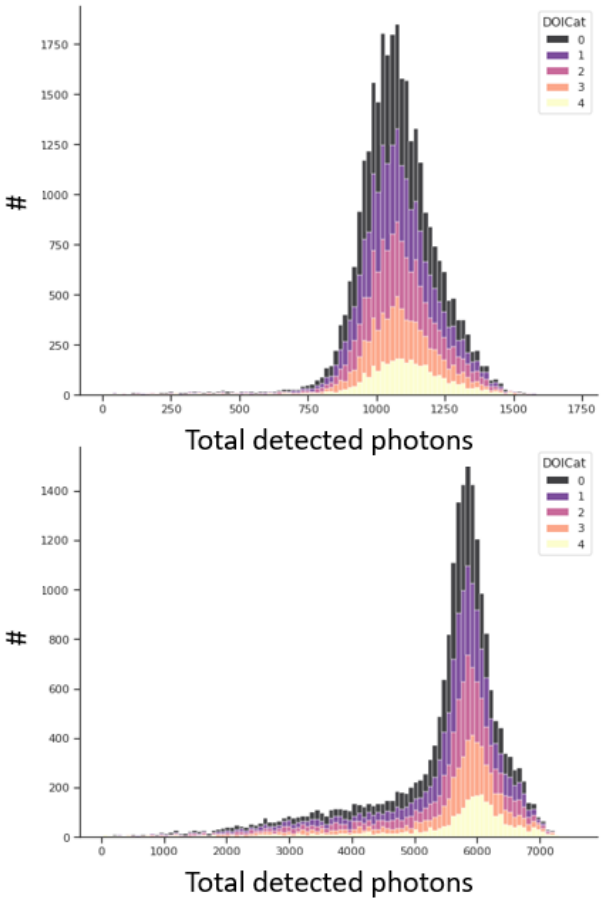

Fig. 5; Distribution of total detected photons for full absorption events in scenario I (top) and II (bottom).

B. *Comparison of DTR with pixelated detectors*

In figure 6 a comparison of the timestamp distribution between the SMMS and pixelated detectors is presented, for scenarios I and II. The difference in CTR-DTR is of the order of a couple of picoseconds, for both scenarios. Distribution and timing of Scenario I is deviating ~35 ps from the experimental results presented in [22] corresponding to ~280 ps without timewalk correction, for a metascintillator pixel of the same characteristics.

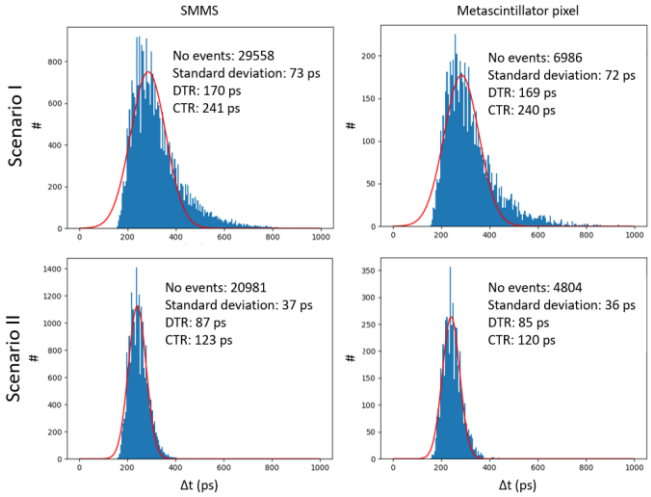

Fig. 6 (Top) Scenario I for SMMS (left) and pixelated (right) configurations; and (bottom) scenario II for SMMS (left) and pixelated (right) configurations.

C. *DOI classification through NN*

The applied fully interconnected NN was a simple un-optimized classifier model, with 8 inputs corresponding to the 8 SiPMs, one hidden layer of 150 perceptrons and outputs, corresponding to the number of DOI layers.

In a first attempt, DOI levels have 3 mm height, leading to 5 layers for scenarios I and II. The results are presented in figure 7 top and middle. For ~10k events organized in a training (8432) and a testing set (2107), the average accuracy reaches 0.7 (scenario I) and 0.85 (Fig. 4), superior to that of FWHM in a Gaussian distribution (~0.75). Scenario III shows reduced average accuracy for 8 DOI layers of 3 mm each, rendering such DOI precision impossible (0.55). At the same time, scenario IV is close to FWHM precision (0.7) and reached 0.74 when the training dataset was switched to a balanced approach (figure 7). An important point when observing DOI classification results is that overall accuracy is not distributed equally over all classes. In particular, highest accuracy is found at the layers closer to the SiPM along with the most distant one. This is presented, in example, along with the confusion map of the balanced approach on scenario IV in figure 7 bottom.

This imbalance is caused by the photon dispersion within the semi-monolithic, which leads to photons in the intermediate but distant classes to have reduced accuracy, in contrast to the ones closer to the SiPM readout side (predominantly direct light), or the first one after gamma entry (back-reflected and direct light add up).

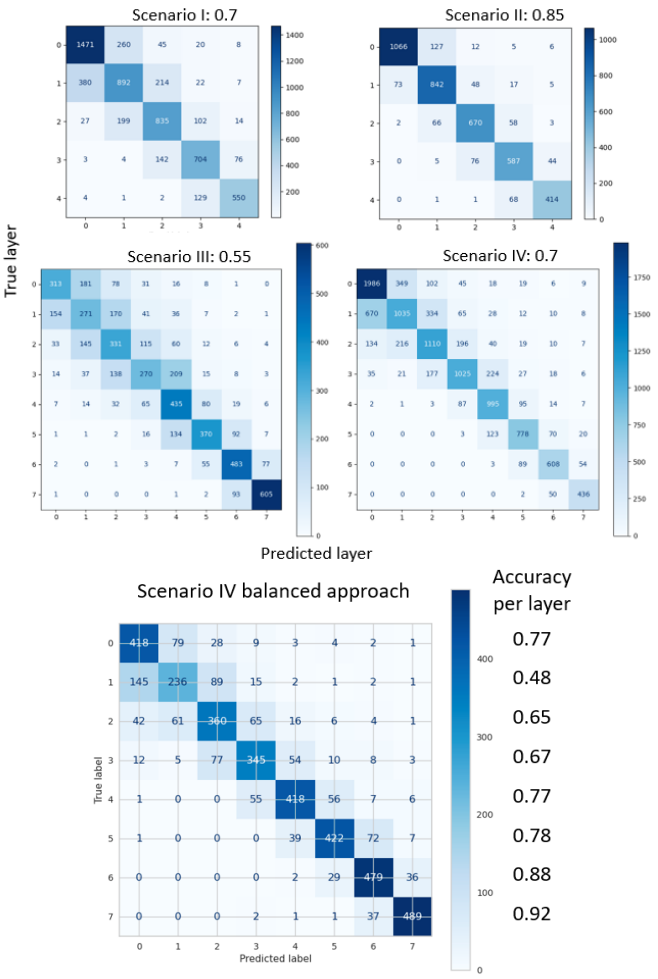

Fig. 7 (Top left) Scenario I, (top right) Scenario II, (middle left) Scenario III, (middle right) Scenario IV confusion maps for 3 mm thick DOI layers; and (bottom) Scenario IV in balanced approach with overall precision 0.74. Variability in accuracy per layer can be observed in the list in right.

As the goal of classification quality equal to FWHM accuracy is far from reached for scenario III, a study of different number of DOI layers was performed. In figure 8 the prediction accuracy for different DOI layers is presented.

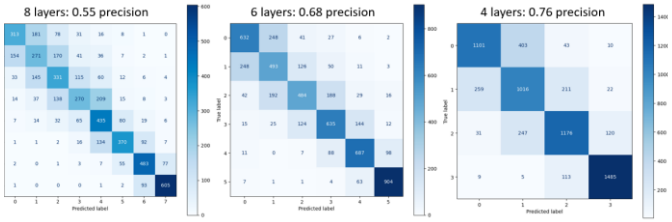

Fig. 8 Scenario III for different DOI segmentations and precision: (left) 8 DOI layers of 3 mm, (middle) 6 DOI layers of 4 mm and (right) 4 DOI layers of 6

D. *DOI regression through NN*

For comparison purposes, DOI was also approached through regression for scenarios III and IV as presented in figure 9. As it can be observed, the variability of prediction accuracy depending on the DOI area persists in this approach as well, as prediction is significantly more accurate closer to the photosensor. A metric, similar to the average accuracy in the classification case is ineffective. This is because such metric does not represent the accuracy distribution through the length of the structure. For this reason, the KPI of DTR improvement through a DOI-driven timewalk correction has been used (figure 10).

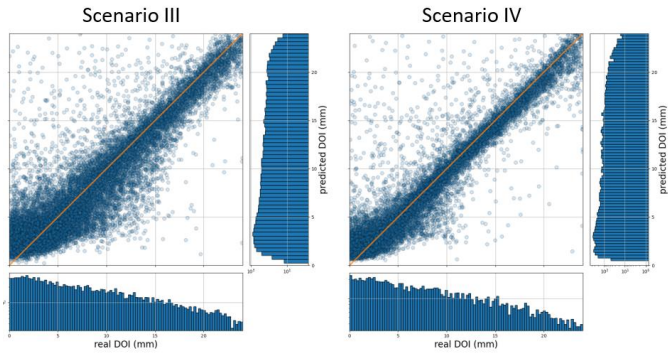

Fig. 9 Regression based DOI prediction for scenarios III and IV.

E. *DOI-driven timewalk correction*

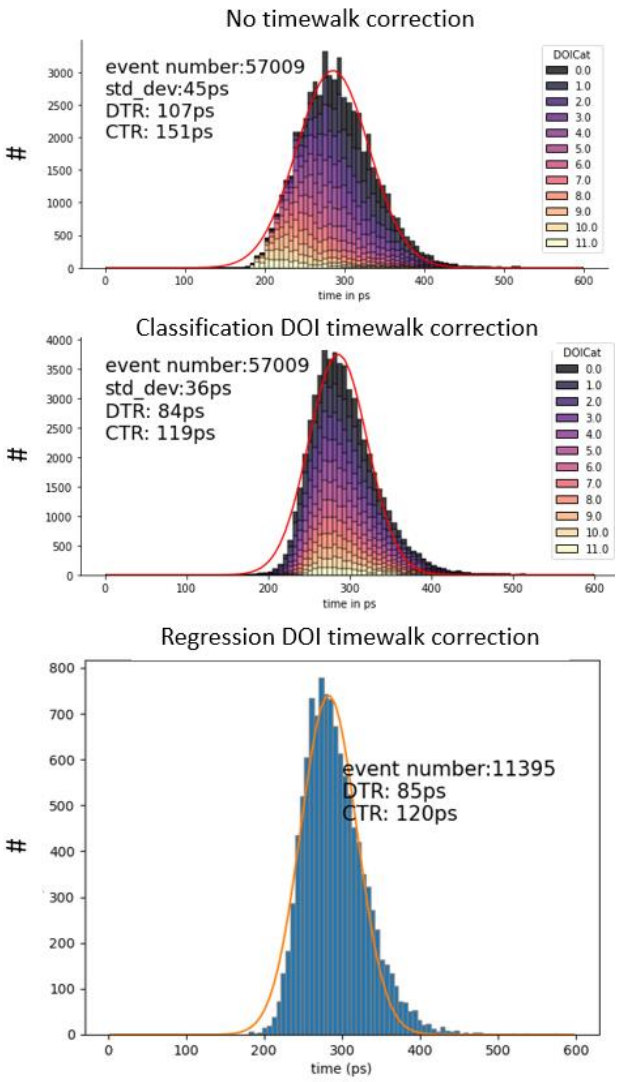

Fig. 10 DOI-driven timewalk corrections for a 3 mm classification (middle) and a regression (bottom) NN approach for scenario IV.

The synergy between TOF and DOI was investigated through a DOI-driven timewalk correction. The first approach was based on the classification results of the previous section. By plotting events according to their DOI, it is possible to observe the expected relation between DOI and photon detection time (figure 10 for scenario IV). This is further denoted by the mean value presented in the plot. By aligning these mean values, it is possible to produce a significantly improved DTR. In particular, for scenario IV the calculated CTR value is 120 ps. The improvement through the application of DOI driven timewalk correction for all scenarios is presented in table 2. In the same figure a DOI-driven timewalk correction is also placed, based on the DOI prediction of a regression model. The KPI of DTR shows similar performance for both regression and classification NN approaches.

TABLE II

TIMEWALK CORRECTION FOR ALL SCENARIOS

SCENARIO INDEX NUMBER	RAW DATA CTR	TIMEWALK CTR	IMPROVEMENT
I	244 ps	225 ps	8%
II	123 ps	107 ps	13%
III	292 ps	253 ps	13%
IV	153 ps	120 ps	22%

F. *Energy spectrums*

In figure 11 the energy spectra are presented for scenarios III and IV. The corresponding energy resolution is 25.5% and 14.5%, respectively. Similar results are seen for scenarios I and II. To be noted that the second corresponds to a feature similar to a photopeak, which however includes only events with none or only limited energy sharing. This can be better understood if this is compared with the spectra of figure 4. Full-absorption events with significant energy sharing have the same effective light yield as not-shared scattered ones.

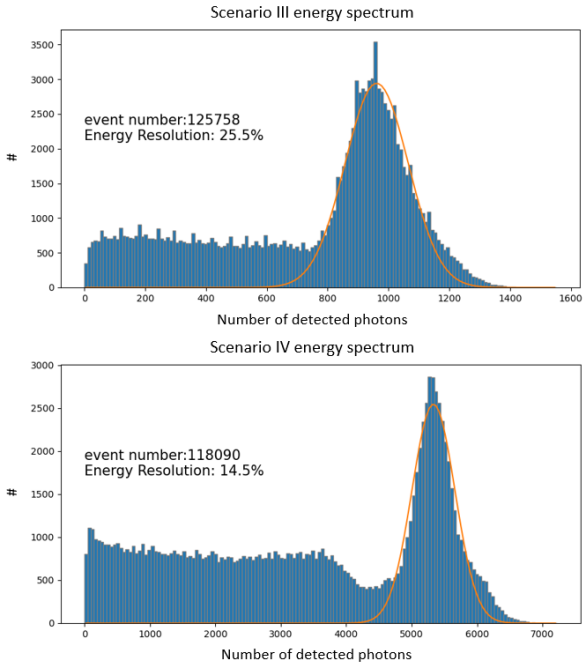

Fig. 11 Energy spectrums for scenarios III and IV at top and bottom, respectiverly.

G. *Energy sharing*

Energy sharing was tackled in particular for scenarios III (figure 12 top) and IV (figure 12 bottom), through the application of a regression NN model. The plots on the left correspond to histograms showing the deviation of prediction from the known value as a percentage of that value. The plots on the right correspond to scatter plots of real versus predicted values, demonstrating the distance from the mean (red line) which shows the correct prediction. The energy sharing resolutions are 16% and 9.5%, for scenario III and IV, respectively. These are significantly better that the calculated energy resolution of the previous section. This can be attributed to the fact the NN has access to not only the number of photons, but their spatial distribution with 3 mm transverse resolution. In this sense, the NN can provide more advanced mechanisms in estimating energy related quantities per event, than the simple addition corresponding to the traditional energy histogram as in figure 11. Scenarios I and II lead to slightly improved results.

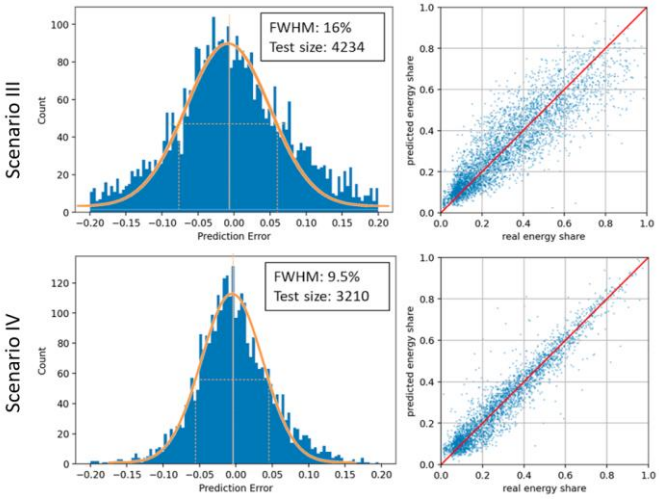

Fig. 12 Energy sharing for scenarios III (top) and IV (bottom): (left) histograms of prediction error for all events and (right) scatter plots of real versus predicted energy sharing values.

H. *Reconstruction of energy of interaction*

Since the classification of events as fully absorbed or scattered is very imbalanced, this problem was approached through a regression NN model. The results are presented in figure 13 left, presenting exponential scale histograms of real and predicted values along with the scatter plot, for scenario III. This demonstrates that the question of energy of interaction can be confidently addressed with this application for a scenario where light yield of the composing metascintillator materials is approximately the same.

Based on such plots, event classification can be achieved with the use of energy thresholds. In table 3 this is presented for three such thresholds, namely 350 keV, 400 keV and 450 keV. These tables serve as confusion maps for this post-regression classification approach. A parameter to evaluate the overall precision is the percentage of true over all events. This parameter reaches values above 95%, corresponding to 2 standard deviations.

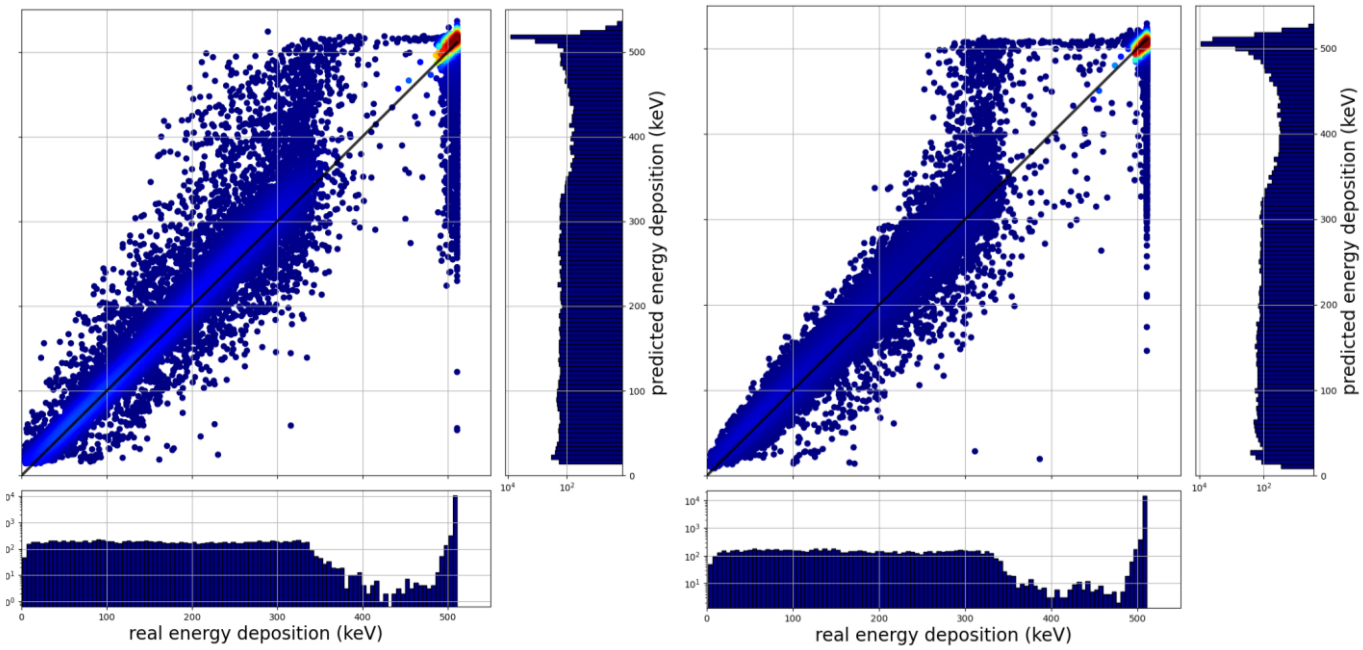

Fig. 13 Density color-coded scatter plot of energy deposition demonstrating the precision of prediction of the regression NN model, for scenario III (left) and scenario IV (right). Bottom and right, corresponding real and predicted energy deposition histograms are presented in exponential scale.

TABLE III

INTERACTION ENERGY-BASED CLASSIFICATION OF EVENTS FOR SCENARIO III

FILTER ENERGY	450 KEV	400 KEV	350 KEV
Correctly estimated fully absorbed	14947	15194	15390
Underestimated fully absorbed (%)	486 (3.1)	303 (1.9)	202 (1.3)
Overestimated scattered (%)	306 (2.9)	403 (3.9)	564 (5.5)
Correctly estimated scattered	10205	9958	9762
Overall precision	96.85%	97.19%	96.95%

The same approach has been undertaken for scenario IV, where light yield of the composing materials is an order of magnitude different. Overall precision is similarly high as in scenario III, above 95% (table IV). The scatter plot of real versus predicted energy deposition values is shown in figure 13 right. Similar results of precision are seen for scenarios I and II.

TABLE IV

INTERACTION ENERGY-BASED CLASSIFICATION OF EVENTS FOR SCENARIO IV

FILTER ENERGY	450 KEV	400 KEV	350 KEV
Correctly estimated fully absorbed	10680	11037	11320
Underestimated fully absorbed (%)	646 (5.7)	315 (2.7)	209 (1.8)
Overestimated scattered (%)	386 (2.9)	715 (5.4)	1011 (7.6)
Correctly estimated scattered	12938	12581	12298
Overall precision	95.73%	95.64%	94.83%

IV. DISCUSSION-FUTURE PLANS

The work presented in this paper corresponds to an extended simulation study which was further improved during its development. The current version of the simulator can be considered a digital twin of the SMMS detector, as all significant phenomena of the detector, including SiPM and electronics, are well understood and included. Nevertheless, the simulator is only the training ground for better understanding and development of the scintillation process in the SMMS. Yet, we consider likely that the developed algorithms and prediction models will find good application in experimental results [23].

The SMMS is a novel and high-performance approach in block scintillator detectors, as it allows unprecedented insight in the spatial distribution of the scintillation event onset, without any mechanical features such as for instance a pixelated multilayer stack [24] or sub-surface laser engraving [25]. In contrast, the stack of different materials, fundamental in the concept of metascintillators, leads to improved timing and carries the synergistic advantage of providing DOI, as demonstrated by these simulations. This architecture is tested using commercially available plastic as the fast material, however the main purpose is to prepare the algorithmic development for the future physical development of 2nd and 3rd generation of metascintillators [26]. In that case, the fast material can be anything from wholly devices hyperbolic metamaterials to scintillating nanoplatelet-loaded plastic or photonic crystal slabs [27]. Whatever the new material to be used, the way to analyze events as presented in this work finds direct application. This sprouts from the fact that even for an order of magnitude difference in light yield, event separation in scattered or photoelectric and precise detection of energy sharing has been possible.

The quest for optimized CTR has not been the focus of this work, as can be demonstrated by the lack of Cherenkov photon production in the used physics list. CTR optimization has been analytically researched in previous publications and is very much dependent on the matching between the scintillator structure and SiPM, read-out and data acquisition systems.

Nevertheless, an effort has been made to demonstrate the increased synergy between DOI and CTR optimizations, by including an analysis on DOI-driven timewalk correction which shows significant improvements of CTR up to 21%. A generalized framework on NN application is also unfortunately not possible, given again how the characteristics of the rest of the detector affect the information channels available. However, within the SMMS concept, work is ongoing to unify all timewalk corrections, including related with DOI, energy-sharing observed non-linearity of the photon count with energy, into one generalized approach with focus on improved CTR. This will be presented in future publications.

We have initially addressed the problem of DOI identification as a classification problem, in the intention to create clearly defined virtual detector elements of dimension 3x3x3 mm^3. Such elements eliminate the parallax error and provide better defined LORs, which significantly improve the spatial resolution of the whole system. Evaluation of this effect is ongoing within a framework of system level simulation with metascintillators [28]. However, an effort has also been made to address DOI identification as a regression problem, trying to define the exact DOI value. This approach is expected to optimize the dimensions of DOI to the minimum possible, while providing more precise values for the aforementioned timewalk correction. Moreover, DOI layers need not have the same size, but can be optimized to have dimensions above a certain confidence threshold such as 0.75, equivalent to the FWHM of a gaussian distribution. Bigger or more balanced datasets could lead to improved results, while the possibility of predicting directly the virtual detector element, as an x-y-z space inside the SMMS, if enough data become available, is also expected to lead to a more precise model.

BGO based systems seem to perform significantly worse than LYSO:Ce based ones in relation with DOI classification and photon population evaluation (for instance figures 4, 6, 8 and 11). This issue is expected, given the generally lower light yield of BGO which leads to reduced number of photons, along with its high refractive index, which limits extraction. In a medium with the dimensions of the semi-monolithic plate, photons need to travel longer paths in the BGO until they are extracted, meaning that a significant number of these is absorbed. This variability leads to a significant spread and reduction of energy resolution, but also to reduced NN performance. Variable surface treatment and extraction facilitating media could improve this issue.

Using the same easily retrieved values of total charge and timestamp per SiPM, it has been possible to provide a significantly more accurate estimation of the extent of energy sharing. Most importantly, through this, it has been possible to provide a precise estimation of energy of interaction in complex metascintillators. This estimation is significantly better than the measured energy resolution provided from direct addition of the SiPM charges, as expressed in detected photon numbers. In this sense, this work opens the discussion on defining the classification of scattered and fully absorbed interactions as a percent quality score of a confusion map. In the specialized issue of PET LOR assignment, energy resolution becomes an obsolete metric, as the only interest in this case is to correctly classify events, something that is achieved significantly better with the application of NN. The same approach will be attempted in experimental measurements of SMMS. We believe that this improves the quality of the detector, through expanding the events amount that have been correctly characterized and thus improving detector sensitivity. Further to that, energy sharing definition allows for the isolation of ultrafast subsets, which can be used as priors for reconstruction in a multi-kernel approach. Work on this direction has also already started.

Using easily obtainable information allows for the NN approach to be generalized in preparation for application on full PET systems. In order to reduce the computational load, NN can be applied directly at the front-end, for instance within the data acquisition chain FPGAs [29]. Calibration runs can be programmed to take place periodically, to improve model quality through adaptation to exact acquisition conditions. In combination with metascintillator subset characterization, the traditional 1 to 1 detector coincidence, which was used for sinograms and reconstruction, is now becoming a complex vector which includes various kernels of timing along with several DOI levels. This computational upgrade can only be tackled, in order to allow fast acquisition and dynamic imaging, with specialized intelligence in the front-end detector. This challenge is necessary both for metascintillators and Cherenkov-driven event time tagging [30]. In this sense, the next step in order to bring system level capabilities to the new generation of detectors is to study and specialize the data acquisition system for metascintillator read-outs, both on ASIC and FPGA levels.

Metascintillator development is moving forward on several fronts: DAQ; scintillating component structuration; new scintillating materials; dedicated signal processing; and multi-kernel image reconstruction. With the presented framework we add an important stepping stone for the second (structuration) and fourth (signal processing) of these directions. To facilitate adoption of the metascintillator, or more generally, variable resolution scintillator paradigms, we intend to publish a library of modular and adaptable analytic and machine learning functions, specialized in the specifics of these detectors. We believe that on the way to 10 ps CTR resolution, there is no other viable alternative than combining all of the above. A new paradigm for PET detector, requires reimagining the whole PET image concept. The advantages have been well described in literature [8].

V. Conclusions

This work presents a simulation of a novel scintillator architecture, the semi-monolithic metascintillator. We prove that this configuration bridges the advantages of two worlds, combining DOI information from the semi-monolithic with pixel-like CTR. The simulation model's accuracy has been compared with experimental results of the same system, showing a less than 15% discrepancy. This model includes the whole physical process from the nuclear gamma interactions, recoil electron energy release, scintillation photon production and propagation and higher order characteristics such as PDE, SPTR and realistic light wavelength sensitivity.

The use of NN has been generalized to address important event characteristics, such as DOI and energy sharing, which are significantly improving precision and effective sensitivity

of the detector. These NN receive input quantities that are easily retrieved from system level detector deployment, such as the total charge and timestamp per SiPM. In this sense, this approach paves the way for experimental application of the developed NN models.

With the predictions retrieved with this simple and light-weight NN model and some analytic corrections, we achieve a 107 ps CTR and <3 mm DOI for an LYSO:Ce-EJ232Q SMMS of 15 mm length, applicable in small animal PET designs and 120 ps and same DOI for the sam configuration of 24 mm.

Energy sharing is successfully predicted through NN, without requirements for any enhancement on the readout scheme such as the ones described in previous works. Precision of energy of interaction estimation exceeds 95%. The new approach is applicable for all energy sharing scenarios, including ones based on LYSO:Ce and fast emitters with significantly lower light yield.

VI. Acknowledgements

All authors declare that they have no known conflicts of interest in terms of competing financial interests or personal relationships that could have an influence or are relevant to the work reported in this paper.

References

[1] Cherry, S. R., Jones, T., Karp, J. S., Qi, J., Moses, W. W., & Badawi, R. D. (2018). Total-body PET: maximizing sensitivity to create new opportunities for clinical research and patient care. Journal of Nuclear Medicine, 59(1), 3-12.

[2] Alberts, I., Hünermund, J. N., Prenosil, G., Mingels, C., Bohn, K. P., Viscione, M., ... & Rominger, A. (2021). Clinical performance of long axial field of view PET/CT: a head-to-head intra-individual comparison of the Biograph Vision Quadra with the Biograph Vision PET/CT. European journal of nuclear medicine and molecular imaging, 48, 2395-2404.

[3] De Ponti, E., Crivellaro, C., Morzenti, S., Monaco, L., Todde, S., Landoni, C., ... & Guerra, L. (2022). Clinical application of a high sensitivity BGO PET/CT scanner: effects of acquisition protocols and reconstruction parameters on lesions quantification. Current Radiopharmaceuticals, 15(3), 218-227.

[4] Kang, H. G., Tashima, H., Wakizaka, H., Nishikido, F., Higuchi, M., Takahashi, M., & Yamaya, T. (2022). Submillimeter resolution positron emission tomography for high-sensitivity mouse brain imaging. Journal of Nuclear Medicine.

[5] Konstantinou, G., Lecoq, P., Benlloch, J. M., & Gonzalez, A. J. (2021). Metascintillators for ultrafast gamma detectors: A review of current state and future perspectives. IEEE Transactions on Radiation and Plasma Medical Sciences, 6(1), 5-15.

[6] Wang, Z., Cao, X., LaBella, A., Zeng, X., Biegon, A., Franceschi, D., ... & Goldan, A. H. (2022). High-resolution and high-sensitivity PET for quantitative molecular imaging of the monoaminergic nuclei: A GATE simulation study. Medical Physics.

[7] He, X., Trigila, C., Ariño-Estrada, G., & Roncali, E. (2022). Potential of Depth-of-Interaction-Based Detection Time Correction in Cherenkov Emitter Crystals for TOF-PET. IEEE Transactions on Radiation and Plasma Medical Sciences.

[8] Lecoq, P., Morel, C., Prior, J. O., Visvikis, D., Gundacker, S., Auffray, E., ... & Benoit, M. (2020). Roadmap toward the 10 ps time-of-flight PET challenge. Physics in Medicine & Biology, 65(21), 21RM01.

[9] Freire, M., Barrio, J., Cucarella, N., Valladares, C., Gonzalez-Montoro, A., de Alfonso, C., ... & Gonzalez, A. J. (2022). Position estimation using neural networks in semi-monolithic PET detectors. Physics in Medicine & Biology, 67(24), 245011.

[10] S. Jan et al. "GATE: a simulation toolkit for PET and SPECT", Phys. Med. Biol. 49 (2004) 4543-4561.

[11] https://www.crystals.saint-gobain.com/files/881/download, retrieved 08.03.2023

[12] https://www.crystals.saint-gobain.com/files/571/view, retrieved 08.03.2023

[13] https://eljentechnology.com/products/plastic-scintillators/ej-232-ej-232q, retrieved 08.03.2023

[14] Gola, A., Acerbi, F., Capasso, M., Marcante, M., Mazzi, A., Paternoster, G., ... & Zorzi, N. (2019). NUV-sensitive silicon photomultiplier technologies developed at Fondazione Bruno Kessler. Sensors, 19(2), 308.

[15] Konstantinou, G., Latella, R., Moliner, L., Zhang, L., Benlloch, J. M., Gonzalez, A. J., & Lecoq, P. (2023). A proof-of-concept of cross-luminescent metascintillators: testing results on a BGO: BaF2 metapixel. Physics in Medicine & Biology, 68(2), 025018.

[16] Gain, U., & Hotti, V. (2021, February). Low-code AutoML-augmented data pipeline–a review and experiments. In Journal of Physics: Conference Series (Vol. 1828, No. 1, p. 012015). IOP Publishing.

[17] Seiffert, U. (2001, April). Multiple layer perceptron training using genetic algorithms. In ESANN (pp. 159-164).

[18] Pal, M. (2005). Random forest classifier for remote sensing classification. International journal of remote sensing, 26(1), 217-222.

[19] Chen, T., He, T., Benesty, M., Khotilovich, V., Tang, Y., Cho, H., ... & Zhou, T. (2015). Xgboost: extreme gradient boosting. R package version 0.4-2, 1(4), 1-4.

[20] Singh, P., Manure, A., Singh, P., & Manure, A. (2020). Introduction to tensorflow 2.0. Learn TensorFlow 2.0: Implement Machine Learning and Deep Learning Models with Python, 1-24.

[21] Li, Y., Gong, P., Tang, X., Hu, Z., Wang, P., Tian, F., ... & Zhu, X. (2022). DOI correction for gamma ray energy reconstruction based on energy segment in 3D position-sensitive CdZnTe detectors. Journal of Instrumentation, 17(03), T03004.

[22] Konstantinou G., Latella R., Moliner L., Zhang L., Benlloch J.M, Gonzalez A.J., Lecoq P. (2021) Metascintillator pulse feature and shape analysis to detect photoelectric interactions and energy sharing. In 2021 IEEE Nuclear Science Symposium and Medical Imaging Conference (NSS/MIC) (pp. 1-4). IEEE.

[23] Carra, P., Bisogni, M. G., Ciarrocchi, E., Morrocchi, M., Sportelli, G., Rosso, V., & Belcari, N. (2022). A neural network-based algorithm for simultaneous event positioning and timestamping in monolithic scintillators. Physics in Medicine & Biology, 67(13), 135001.

[24] Kang, H. G., Tashima, H., Nishikido, F., Akamatsu, G., Wakizaka, H., Higuchi, M., & Yamaya, T. (2021). Initial results of a mouse brain PET insert with a staggered 3-layer DOI detector. Physics in Medicine & Biology, 66(21), 215015.

[25] Konstantinou, G., Chil, R., Desco, M., & Vaquero, J. J. (2017). Subsurface laser engraving techniques for scintillator crystals: Methods, applications, and advantages. IEEE Transactions on Radiation and Plasma Medical Sciences, 1(5), 377-384.

[26] Konstantinou G., (2023) Chapter: "Metascintillators for ultra-fast gamma detectors" in "Gamma Ray Spectroscopy", Springer publishing, in print

[27] Turtos, R.M., Gundacker, S., Omelkov, S. et al. On the use of CdSe scintillating nanoplatelets as time taggers for high-energy gamma detection. npj 2D Mater Appl 3, 37 (2019). https://doi.org/10.1038/s41699-019-0120-8

[28] Bonifacio, D.A.B., Latella R., Murata H., L.,Benlloch J. M., Gonzalez A. J., Lecoq P. and Konstantinou G. (2023) Analytical model for the sensitivity of a cylindrical PET system based on bulk materials or metascintillators. IEEE Transactions on Radiation and Plasma Medical Sciences- submitted

[29] Mueller, F., Naunheim, S., Kuhl, Y., Schug, D., Solf, T., & Schulz, V. (2022). A semi-monolithic detector providing intrinsic DOI-encoding and sub-200 ps CRT TOF-capabilities for clinical PET applications. Medical Physics.

[30] Kratochwil, N., Auffray, E., & Gundacker, S. (2020). Exploring Cherenkov emission of BGO for TOF-PET. IEEE Transactions on Radiation and Plasma Medical Sciences, 5(5), 619-629.